

Transforming Static Images Using Generative Models for Video Salient Object Detection

Suhwan Cho Minhyeok Lee Jungho Lee Sangyoun Lee

Yonsei University

Abstract

In many video processing tasks, leveraging large-scale image datasets is a common strategy, as image data is more abundant and facilitates comprehensive knowledge transfer. A typical approach for simulating video from static images involves applying spatial transformations, such as affine transformations and spline warping, to create sequences that mimic temporal progression. However, in tasks like video salient object detection, where both appearance and motion cues are critical, these basic image-to-video techniques fail to produce realistic optical flows that capture the independent motion properties of each object. In this study, we show that image-to-video diffusion models can generate realistic transformations of static images while understanding the contextual relationships between image components. This ability allows the model to generate plausible optical flows, preserving semantic integrity while reflecting the independent motion of scene elements. By augmenting individual images in this way, we create large-scale image-flow pairs that significantly enhance model training. Our approach achieves state-of-the-art performance across all public benchmark datasets, outperforming existing approaches. Code and models are available at <https://github.com/suhwan-cho/RealFlow>.

1. Introduction

In deep learning-based image and video processing tasks, the quantity and quality of training data are crucial factors influencing model performance. However, video data introduces additional complexities due to its temporal dimension, making annotation far more labor-intensive and costly compared to image data. To address this challenge, researchers often turn to large-scale, annotated image datasets, which are more accessible and diverse, to support model learning for video tasks. A common strategy for adapting image data to video tasks involves transforming static images and their corresponding annotations (e.g.,

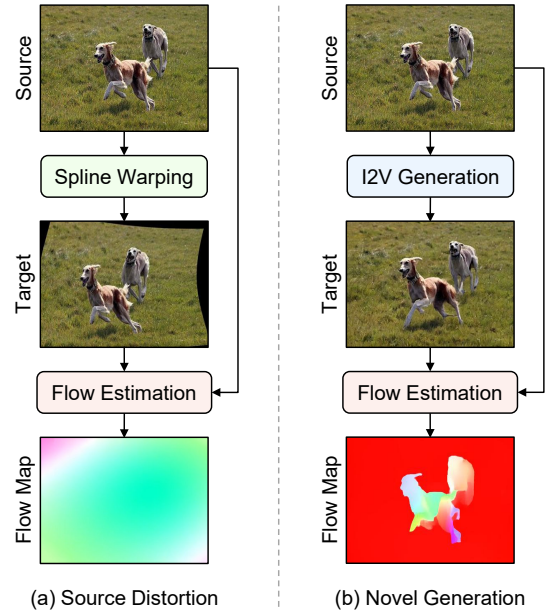


Figure 1. Visualization of the optical flow generation process from a static image using two different target image generation methods.

segmentation masks) to simulate sequences that mimic the temporal progression of video content. Spatial transformations, such as affine transformations and spline warping, are applied to static images to introduce motion cues, thereby generating image sequences that resemble actual video data. This approach has proven effective in video processing, allowing models to learn temporal patterns and structural variations from diverse image data, which helps mitigate the limited availability of video data.

However, this approach falls short in tasks where motion cues are critical. For instance, video salient object detection (VSOD) requires both appearance and motion cues to accurately identify and segment prominent objects in video sequences. VSOD models typically adopt a two-stream approach, incorporating both RGB images and optical flow maps to capture appearance and motion properties simulta-

neously. The flow information provides context for the dynamics of each object, allowing models to distinguish between independent object movement and background motion. Unfortunately, existing image-to-video simulation methods, which rely on simple spatial transformations, fail to generate realistic optical flows, as shown in Figure 1 (a). These transformations neglect the contextual relationships between objects in the scene, resulting in flows that fail to accurately reflect the independent motion properties of individual elements. As a result, these methods fall short in tasks like VSOD, where both appearance and motion cues are essential for accurate segmentation.

To overcome this limitation, we propose a novel solution using image-to-video diffusion models to generate realistic transformations of static images. Diffusion models possess the ability to generate novel images while fully understanding the contextual relationships within them. This enables the generation of plausible optical flows by transforming source images while preserving the semantic integrity of the scene and reflecting the independent motion of each object, as depicted in Figure 1 (b). Unlike traditional spatial transformations, which distort images without accounting for object relationships, our approach maintains these relationships to generate high-quality image-flow pairs. These pairs significantly enhance model training for motion-guided tasks such as VSOD. By augmenting static images with diffusion-based transformations, we can simulate realistic video sequences and generate the corresponding optical flows necessary for effective learning in two-stream models.

We evaluate our method on several public VSOD benchmarks. Unlike previous approaches that rely on complex network architectures, we adopt a simple encoder-decoder framework to demonstrate the effectiveness of our training strategy. Experimental results show that augmenting training data with large-scale image-flow pairs significantly improves model performance. Specifically, we achieve new state-of-the-art \mathcal{S} measure [15] scores of 94.5%, 92.6%, 80.3%, and 96.2% on the DAVIS 2016 [39] validation set, FBMS [34] test set, DAVSOD [16] test set, and ViSal [52] dataset, respectively.

Our main contributions can be summarized as follows:

- We identify the limitations of current image-to-video simulation methods for motion-guided tasks, emphasizing their inability to produce realistic optical flows.
- We demonstrate that image-to-video diffusion models can generate realistic image transformations that preserve contextual relationships, enabling the synthesis of plausible optical flows.
- We show that these image-flow pairs significantly improve VSOD model performance, achieving state-of-the-art results across public benchmark datasets.

2. Related Work

Utilizing image data for video models. To leverage the extensive knowledge embedded in large-scale image datasets, video processing tasks commonly incorporate image data. A straightforward approach is to augment image data with spatial transformations and treat the original and newly generated images as a video sequence.

In video object segmentation (VOS), for instance, MaskTrack [40] learns a semi-supervised VOS network by applying affine transformations and thin-plate spline [4] deformations to the segmentation mask of the query frame. The transformed mask is treated as the mask of the previous frame and used along with the query frame image as a training sample. RGMP [35] adopts a similar approach to MaskTrack, simulating the previous frame’s masks through transformations, while further enriching the diversity of training samples by overlaying foreground objects from salient object detection datasets [9, 45] onto background images from PASCAL-VOC [14, 21]. To create varied training samples, spatial transformations are separately applied to each image, simulating diverse scenarios. Recent methods leverage image data even more directly. Rather than simply approximating conditions encountered during inference, as MaskTrack and RGVI do, these methods generate video-like samples by independently transforming images and their corresponding object masks, then sequencing them temporally. This approach has been shown to be effective across various VOS settings, including both semi-supervised and unsupervised VOS methods [7, 8, 10, 33, 36, 43, 44].

Beyond VOS, using image data is also common in other video tasks. STEm-Seg [2] trains a video instance segmentation model using image instance segmentation datasets, synthesizing training clips with random affine transformations and motion blur effects applied on the fly. FCNS [53] introduces a novel data augmentation technique that simulates video training data from images to learn varied saliency information and mitigate overfitting given the limited availability of training videos.

While these methods effectively implement an image-to-video simulation approach, they rely solely on spatial transformations without accounting for contextual information within each image. As a result, the optical flows generated between the original and transformed images lack meaningful motion cues that could enhance object-level semantics.

Motion-guided architecture. Leveraging motion cues is essential in many video tasks, as it provides crucial insights into the dynamics of each element within images. These cues are typically captured by estimating movement between consecutive frames, incorporating short-term temporal information. This approach is particularly effective in segmentation tasks, as the spatial details preserved in flow maps improve model accuracy in pixel-level prediction.

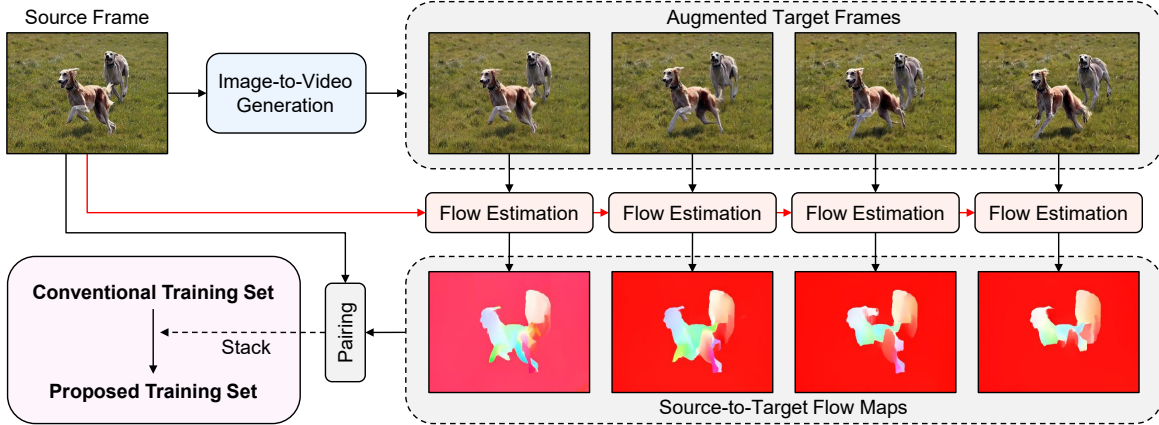


Figure 2. Overview of our training sample simulation process. Starting with a static source image, target images are generated using an image-to-video generation model. Optical flow maps are then estimated between the source and target images, with each map paired with the source image to enrich the training dataset.

MATNet [63] integrates motion information with appearance features through an asymmetric attention block within each encoding layer, transforming appearance features into motion-attentive representations. MGA [31] employs separate modules for salient object detection in still images and motion saliency detection in optical flow maps, adapting these modules to each other through end-to-end training. AMC-Net [57] dynamically balances appearance and motion cues when fusing features from each modality, adjusting feature scaling via gating functions. FSNNet [24] models deep relationships between appearance and motion cues within feature embedding layers, enforcing mutual constraints that enable robust encoding of each modality. PMN [29], GSA-Net [30], and DPA [12] leverage attention mechanisms to fuse appearance and motion cues while capturing temporal relationships along the sequence.

Despite these advancements, motion-guided methods often face limitations due to the scarcity of video training data. While image-to-video simulation techniques strive to produce realistic videos, the optical flows generated from this simulated data lack authentic motion characteristics, reducing their effectiveness for training motion-guided models.

Image-to-video generation. Recently, video generation models have gained significant attention due to their wide-ranging applications in content creation and editing. Among these, image-to-video generation models, which produce videos from single images, have demonstrated superior generation quality and controllability compared to general video generation approaches. By using the given image as an explicit first-frame guide, these models ensure high-quality generation aligned with the desired content.

The advent of diffusion models [23, 41, 46] has greatly advanced image-to-video generation, harnessing the powerful generative capabilities of diffusion. Notable examples of

such approaches include Stable Video Diffusion [3], Gen-2 [42], I2VGen-XL [60], PikaLabs [28], SparseCtrl [20], and SORA [5]. Extending these works, some recent methods add more control by explicitly guiding generation with optical flow or trajectory information [32, 59].

Our objective, however, is purely to transform given images into plausible optical flows. For this purpose, we adopt a straightforward image-to-video architecture that generates natural videos starting from a single image as the first frame, without explicit guidance in the video generation process.

3. Approach

3.1. Transforming Static Images

As shown in Figure 1, spatially distorting the original source image to generate a target frame for optical flow estimation does not yield realistic optical flow maps. To obtain high-quality optical flow maps with video-like properties from static images, we use an image-to-video generation model that generates new frames directly, rather than relying on the distortion of the source image.

Network overview. In the image-to-video generation process, we employ Stable Video Diffusion [3] based on a 3D-UNet [13] architecture. Following recent approaches, a pixel-to-latent conversion is applied before the denoising model, with a latent-to-pixel conversion following it, using a pre-trained VAE [26] encoder and decoder, respectively. Notably, the VAE decoder incorporates 3D convolutional layers to account for the time dimension, thereby ensuring temporal consistency during the decoding process.

Starting from Gaussian noise $x \in \mathbb{R}^{C \times THW}$ and the source image latent $z_s \in \mathbb{R}^{C \times HW}$, the denoised latent $z_t \in \mathbb{R}^{C \times THW}$ is obtained as

$$z_t = \Phi(x, \text{repeat}(z_s, T)), \quad (1)$$

where Φ denotes the denoising 3D-UNet model. The output denoised latent z_t is then decoded with the VAE decoder on a per-frame basis, with each frame representing a transformed image generated from the source image. Note that the number of video frames T is set to 14, following the default setting in Stable Video Diffusion.

Sampling details. During the sampling process, we use 25 steps of the deterministic DDIM sampler [47]. The classifier guidance scale [22] is set to 3.0 for the first frame and 1.0 for the last frame. The resolution and frame rate are set to 576×1024 and 7, in line with the default setting. The decoding chunk size is set to 8 to balance generation quality and computational cost.

3.2. Hallucinating Flows

After generating target images from each source image using the image-to-video generation model, we obtain sets of source-target pairs for network training. Formally, the temporary paired data P can be represented as

$$P_1^T = \{(I_s, I_1), (I_s, I_2), \dots, (I_s, I_T)\}, \quad (2)$$

where I_s represents the source image and I_t denotes the generated target image at each frame $t \in \{1, 2, \dots, T\}$. From these temporary pairs, we construct training samples for network training, as illustrated in Figure 2.

Data creation. In order to obtain the final image-flow pairs to learn the two-stream network for VSOD, we need to estimate flows from the temporary paired data P . For optical flow estimation, we use a pre-trained RAFT model [50] while maintaining the original image resolution. Formally, the final paired data Q can be obtained as

$$Q_1^T = \{(I_s, F_{s \rightarrow 1}), (I_s, F_{s \rightarrow 2}), \dots, (I_s, F_{s \rightarrow T})\}, \quad (3)$$

where $F_{A \rightarrow B}$ indicates the estimated optical flow map from frame A to frame B . Note that the paired data Q is obtained for each static image separately, and therefore, from N source images, we can obtain NT paired data samples.

Dataset construction. We adopt the DUTS [51] dataset as the source for applying our data creation protocol, which consists of 10,553 training images and 5,019 testing images. Since these image samples are used solely for network training, we utilize the entire training and testing sets to construct our training dataset. For each static image from DUTS, T image-flow samples are extracted, resulting in a total of 15,572 data pairs for training. Note that, as the flows are calculated using the source image as the starting frame for optical flow estimation, the RGB images, segmentation masks, and optical flows are all spatially aligned. These data pairs are then combined with conventional training pairs to enhance data diversity during network training.

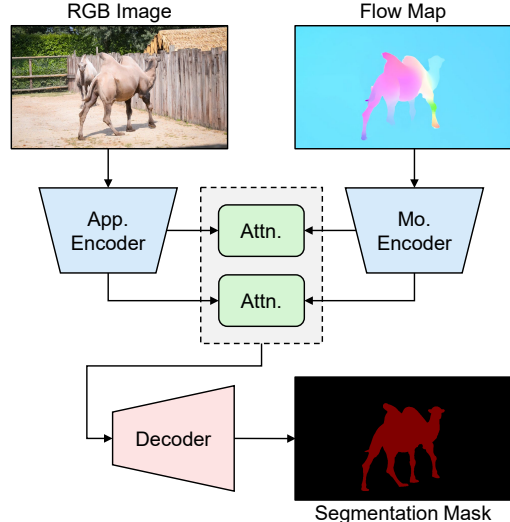


Figure 3. Visualization of our two-stream network architecture, which uses both RGB images and optical flow maps as input for primary object mask prediction.

3.3. Segmentation Model

With the aid of our simulated training samples, we train a VSOD network to detect primary objects at the pixel level. Following conventional flow-guided object segmentation approaches, we design our model using a two-stream architecture, as shown in Figure 3.

Network architecture. Our network includes dual encoders designed to capture appearance cues from RGB images and motion cues from optical flow maps. Both encoders are based on MiT-b2 [56], utilizing only its encoder component. After embedding each modality, multi-level features are fused through simple attention blocks [55]. The fused features are then passed through the decoder, where they are progressively decoded by combining feature interpolation with skip connections. Following the decoding process, a binary segmentation mask representing the primary objects is obtained.

Network training. The segmentation network is trained using a straightforward supervised learning protocol. We employ cross-entropy loss and the Adam optimizer [27], with a fixed learning rate of $1e-5$, a batch size of 16, and an input resolution of 512×512 . The training is conducted on two GeForce RTX TITAN GPUs, each utilizing less than 16GB of GPU memory. The entire network training process takes approximately two days on this hardware. During training, we combine both actual video data and simulated data derived from static images. Specifically, the actual data consists of the DAVIS 2016 [39] and DAVSOD [16] training sets. The data samples are randomly shuffled, with the mixture ratio set to 2:1:1 for simulated data, DAVIS 2016 data, and DAVSOD data, respectively.

Table 1. Quantitative evaluation on the DAVIS 2016 validation set, FBMS test set, DAVSOD test set, and ViSal dataset. Scores marked in red indicate the highest score, while scores marked in blue represent the second-highest score.

Method	DAVIS 2016			FBMS			DAVSOD			ViSal			Average		
	$\mathcal{S} \uparrow$	$\mathcal{F} \uparrow$	$\mathcal{M} \downarrow$	$\mathcal{S} \uparrow$	$\mathcal{F} \uparrow$	$\mathcal{M} \downarrow$	$\mathcal{S} \uparrow$	$\mathcal{F} \uparrow$	$\mathcal{M} \downarrow$	$\mathcal{S} \uparrow$	$\mathcal{F} \uparrow$	$\mathcal{M} \downarrow$	$\mathcal{S} \uparrow$	$\mathcal{F} \uparrow$	$\mathcal{M} \downarrow$
SSAV [16]	89.3	86.1	2.8	87.9	86.5	4.0	72.4	60.3	9.2	94.3	93.9	2.0	86.0	81.7	4.5
AD-Net [58]	-	80.8	4.4	-	81.2	6.4	-	-	-	-	90.4	3.0	-	-	-
F ³ Net [54]	85.0	81.9	4.1	85.3	81.9	6.8	68.9	56.4	11.7	87.4	90.7	4.5	81.7	77.7	6.8
MINet [37]	86.1	83.5	3.9	84.9	81.7	6.7	70.4	58.2	10.3	90.3	91.1	4.1	82.9	78.6	6.3
GateNet [61]	86.9	84.6	3.6	85.7	83.2	6.5	70.1	57.8	10.4	92.1	92.8	3.9	83.7	79.6	6.1
PCSA [19]	90.2	88.0	2.2	86.6	83.1	4.1	74.1	65.5	8.6	94.6	94.0	1.7	86.4	82.7	4.2
DFNet [62]	-	89.9	1.8	-	83.3	5.4	-	-	-	-	92.7	1.7	-	-	-
3DC-Seg [33]	-	91.8	1.5	-	84.5	4.8	-	-	-	-	92.2	1.9	-	-	-
CASNet [25]	87.3	86.0	3.2	85.6	86.3	5.6	69.4	-	8.9	82.0	84.7	2.9	81.1	-	5.2
FSNet [24]	92.0	90.7	2.0	89.0	88.8	4.1	77.3	68.5	7.2	-	-	-	-	-	-
CFAM [6]	91.8	90.9	1.5	90.9	91.5	2.6	75.3	66.2	8.3	94.7	95.1	1.3	88.2	85.9	3.4
UFO [49]	91.8	90.6	1.5	89.1	88.8	3.1	-	-	-	95.9	95.1	1.3	-	-	-
DBSNet [17]	92.4	91.4	1.4	88.2	88.5	3.8	77.8	68.8	7.6	93.1	92.8	2.0	87.9	85.4	3.7
HFAN [38]	93.4	92.9	0.9	87.5	84.9	3.3	75.3	68.0	7.0	94.1	93.5	1.1	87.6	84.8	3.1
TMO [11]	92.8	92.0	0.9	88.6	88.2	3.1	76.7	70.8	7.2	94.2	94.7	1.0	88.1	86.4	3.1
OAST [48]	93.5	92.6	1.1	91.7	91.9	2.5	78.6	71.2	7.0	94.8	95.0	1.0	89.7	87.7	2.9
TGFormer [18]	93.2	92.2	1.1	91.6	91.9	2.6	79.8	72.8	6.5	95.2	95.5	1.1	90.0	88.1	2.8
RealFlow	94.5	93.9	1.0	92.6	90.6	2.8	80.3	73.2	6.6	96.2	96.6	1.0	90.9	88.6	2.9

4. Experiments

This section outlines the datasets and evaluation metrics used to validate our approach. We then quantitatively and qualitatively compare our method to other state-of-the-art methods and analyze it through additional experiments. All evaluations are conducted on a single GeForce RTX 2080 Ti GPU. Our VSOD network, trained with realistic simulated image-flow pairs, is referred to as RealFlow.

4.1. Datasets

We use four widely adopted VSOD datasets: DAVIS 2016 [39], FBMS [34], DAVSOD [16], and ViSal [52]. For each video, optical flows are precomputed between consecutive frames using RAFT [50] and saved alongside the RGB images and segmentation masks.

DAVIS 2016. A primary VSOD benchmark, the DAVIS dataset includes 50 videos with densely annotated segmentation masks for every frame. Of these, 30 videos are designated for training and 20 for validation. We incorporate the training set into our data for model training.

FBMS. The FBMS dataset contains 59 videos, with 29 for training and 30 for validation. Due to sparse frame annotations, only the annotated frames are used. Consistent with VSOD protocols, we exclude its training set from our data.

DAVSOD. The DAVSOD dataset, a recent benchmark in VSOD, comprises 61 training videos and 35 test videos, with full annotations for each frame. We include its training set in our training data.

ViSal. The ViSal dataset consists of 17 videos with 193 annotated frames, though only selected frames are labeled. Since it lacks a defined training and testing split, we use it solely for evaluation.

4.2. Evaluation Metrics

We adopt three evaluation metrics to quantitatively validate the effectiveness of our approach: \mathcal{S} [15], \mathcal{F} , and \mathcal{M} .

\mathcal{S} measure. The \mathcal{S} measure evaluates structural similarity between the predicted saliency map and the ground truth segmentation mask, calculated as

$$\mathcal{S} = \alpha \mathcal{S}_o + (1 - \alpha) \mathcal{S}_r, \quad (4)$$

where \mathcal{S}_o represents object-aware structural similarity and \mathcal{S}_r represents region-aware structural similarity. Following existing approaches, α is set to 0.5.

\mathcal{F} measure. The \mathcal{F} measure is based on the precision and recall of the predicted saliency map, calculated as

$$\mathcal{F} = \frac{(1 + \beta^2) \times \text{Precision} \times \text{Recall}}{\beta^2 \times \text{Precision} + \text{Recall}}, \quad (5)$$

where β^2 is set to 0.3 following [1].

\mathcal{M} measure. The \mathcal{M} measure calculates the average pixel-wise difference between the saliency prediction and the ground truth mask. Formally, it is represented as

$$\mathcal{M} = \frac{\sum_{p=1}^H \sum_{q=1}^W |M_{pred}^{p,q} - M_{gt}^{p,q}|}{H \times W}, \quad (6)$$

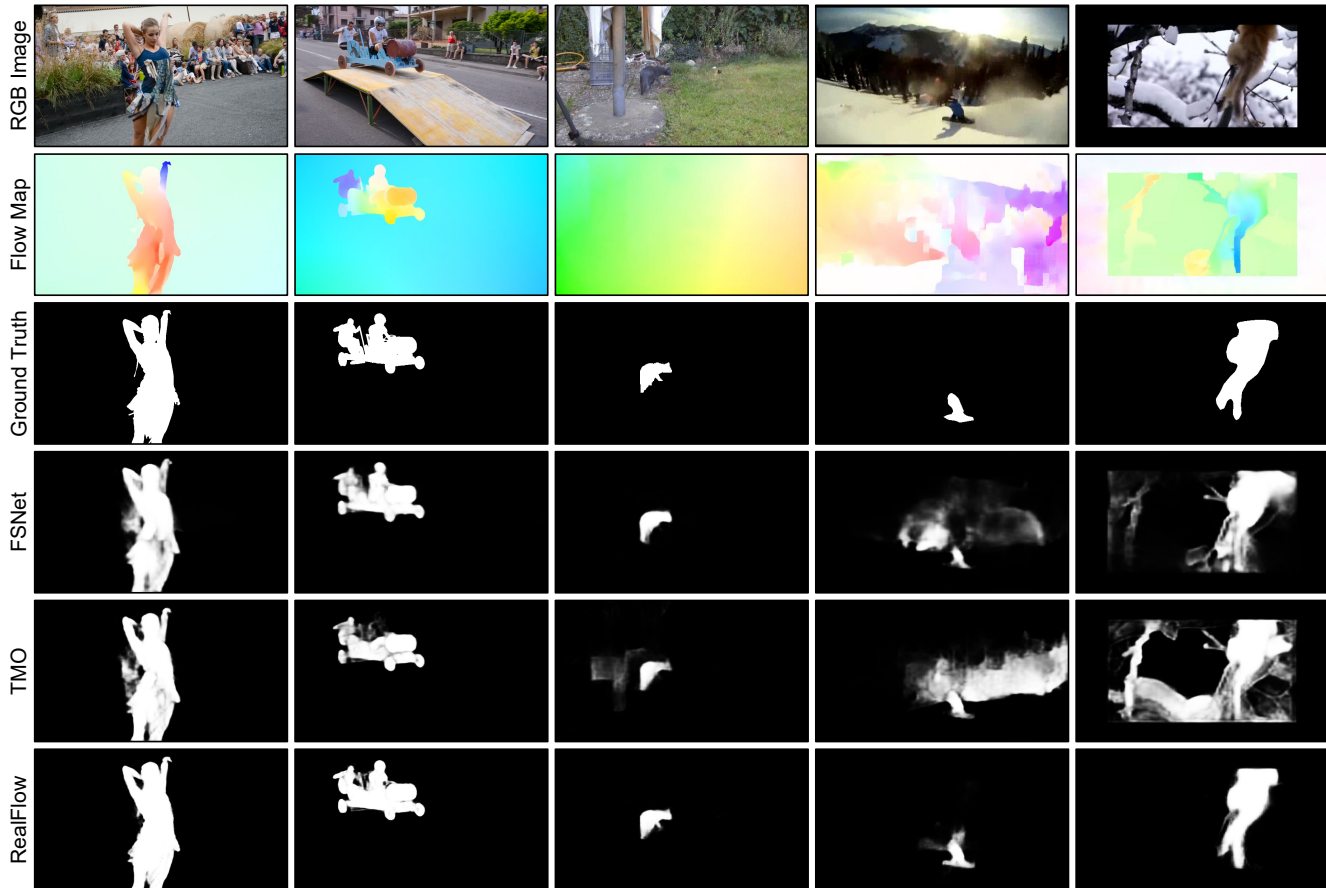


Figure 4. Qualitative comparison between state-of-the-art methods and the proposed RealFlow.

where M_{pred} and M_{gt} denote the predicted saliency map and the ground truth mask, respectively; H and W represent the image height and width, and p and q indicate individual pixel locations along the height and width dimensions.

4.3. Quantitative Results

We compare our approach against existing state-of-the-art methods on the DAVIS 2016 [39] validation set, FBMS [34] test set, DAVSOD [16] test set, and ViSal [52] dataset, as presented in Table 1. For a comprehensive view, we also report the average score across these four datasets for each metric. Our method achieves the highest \mathcal{S} measure [15] score on all benchmark datasets, surpassing prior methods by a substantial margin. The \mathcal{F} measure performance is similarly strong, achieving the top score on three of the four benchmarks. For the \mathcal{M} measure, our approach demonstrates competitive performance, reaching accuracy levels comparable to other leading methods. These results indicate that our method offers significant improvements over existing VSOD solutions, delivering high saliency prediction accuracy across all metrics and establishing its effectiveness across diverse scenarios.

4.4. Qualitative Results

In Figure 4, we compare our approach with state-of-the-art methods FSNet [24] and TMO [11] across varied VSOD scenarios. In the first two columns, where primary objects are well-aligned with optical flow maps, our method delivers sharper and more precise segmentation, especially along object edges, surpassing existing methods. The third column shows cases with minimal object movement relative to the background, where our network effectively leverages RGB appearance cues to accurately capture primary objects. The fourth and fifth examples depict scenes with substantial motion and noisy optical flow maps, which confuse other methods. In contrast, our approach remains robust, accurately segmenting primary target objects even in complex motion scenarios.

4.5. Analysis

In this section, we conduct a series of experiments to provide a deeper analysis of the proposed approach, offering additional insights and intuitions into its effectiveness. These experiments aim to deliver a comprehensive under-

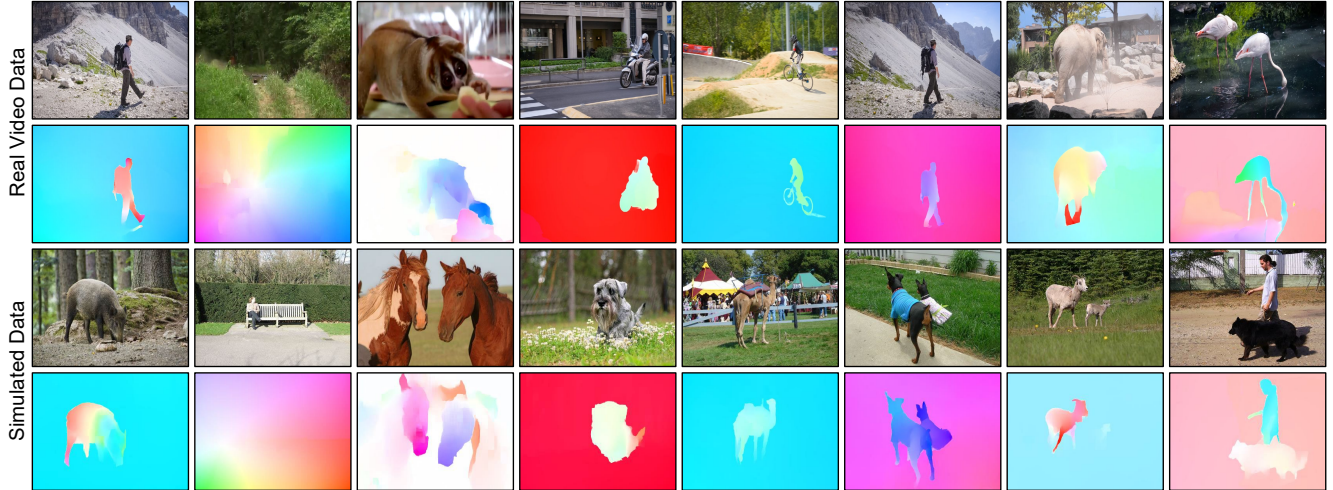


Figure 5. Aligned qualitative comparison between real video data and our simulated data.

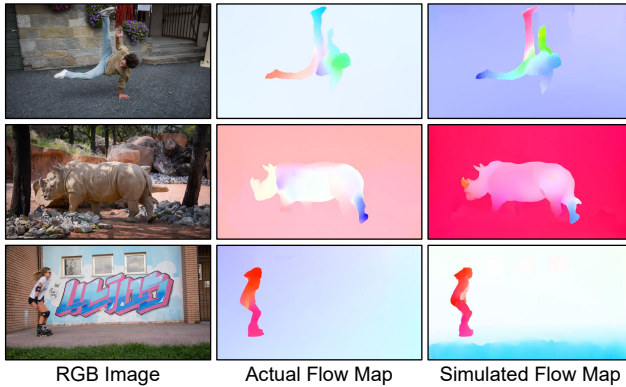


Figure 6. Direct qualitative comparison of actual and simulated flow maps, both derived from the same source image.

standing of the key properties of our method, highlighting its strengths, limitations, and the underlying mechanisms driving its performance.

Comparison to real data. The goal of our approach is to simulate realistic image-flow pairs that closely mirror those from real video data, thereby improving network training. To evaluate the plausibility of the simulated data, we provide an aligned comparison with real video data in Figure 5. As seen in various examples, the simulated data contains a range of optical flow maps, from explicit flows that capture object shapes to more ambiguous flows with less distinct object information. This demonstrates that the simulated data spans a wide distribution of scenarios, supporting the validity of incorporating it into network training.

Furthermore, we qualitatively compare the actual flow map with our simulated flow map, using the same source image, in Figure 6. The comparison shows that the simulated flow map effectively replicates the desired object

movements within the image, generating plausible optical flow maps for VSOD. This further substantiates the effectiveness and validity of our data simulation strategy.

Training protocol. We validate the effectiveness of our simulated data for network training in Table 2. Notably, the network trained solely on our simulated data outperforms the network trained on real video data, such as the DAVIS 2016 [39] and DAVSOD [16] training sets, on all datasets except the DAVIS 2016 validation set. This result highlights the limitations of existing training data protocols and underscores the quality and effectiveness of our simulated data in building a robust VSOD model. When we combine real video data with our simulated data, we achieve the highest performance across all datasets and metrics, emphasizing the critical role of training data volume in network training.

Backbone network. Table 3 presents a quantitative comparison of different backbone network versions, with evaluation scores averaged across four datasets: DAVIS 2016 [39] validation set, FBMS [34] test set, DAVSOD [16] test set, and ViSal [52] dataset. Our default backbone, MiT-b2 [56], achieves the highest scores across all evaluation metrics, striking an effective balance of inference speed and parameter efficiency suitable for real-time applications. Lighter backbones provide even faster inference speeds and reduced parameter counts, with a minor accuracy trade-off, offering flexibility for applications that prioritize speed or precision. The consistent trend of better scores with larger backbones further reinforces the stability of our method.

Input resolution. Table 4 compares various input resolution settings to evaluate our method in different scenarios. Similar to Table 3, average metric scores are calculated across the four datasets. Each network is re-trained and tested at its specific resolution setting to ensure accurate results. As shown, lower resolutions yield faster infer-

Table 2. Ablation study on the training protocol.

Training	DAVIS 2016			FBMS			DAVSOD			ViSal			Average		
	$S \uparrow$	$\mathcal{F} \uparrow$	$\mathcal{M} \downarrow$	$S \uparrow$	$\mathcal{F} \uparrow$	$\mathcal{M} \downarrow$	$S \uparrow$	$\mathcal{F} \uparrow$	$\mathcal{M} \downarrow$	$S \uparrow$	$\mathcal{F} \uparrow$	$\mathcal{M} \downarrow$	$S \uparrow$	$\mathcal{F} \uparrow$	$\mathcal{M} \downarrow$
Real	93.1	91.6	1.3	85.8	85.5	5.3	76.0	68.7	7.8	94.5	94.4	1.8	87.4	85.1	4.1
Simulated	91.7	89.6	2.0	91.0	89.0	2.9	78.1	70.1	7.8	96.1	96.4	1.1	89.2	86.3	3.5
Mixed	94.5	93.9	1.0	92.6	90.6	2.8	80.3	73.2	6.6	96.2	96.6	1.0	90.9	88.6	2.6

Table 3. Ablation study on the backbone network.

Backbone	fps	Param #	$S \uparrow$	$\mathcal{F} \uparrow$	$\mathcal{M} \downarrow$
MiT-b0	61.1	13.8M	89.4	87.0	3.5
MiT-b1	45.5	33.6M	89.8	87.3	3.2
MiT-b2	29.5	55.7M	90.9	88.6	2.6

Table 4. Ablation study on the input resolution.

Resolution	fps	$S \uparrow$	$\mathcal{F} \uparrow$	$\mathcal{M} \downarrow$
256×256	55.0	90.0	87.5	3.0
384×384	44.2	90.2	87.8	2.9
512×512	29.5	90.9	88.6	2.6

ence speeds with a slight decrease in prediction accuracy. Like the backbone choice, input resolution can be adjusted to balance speed and accuracy based on user needs, making the method adaptable to various application requirements.

Source image deformation. The image-to-video generation model is trained to produce a plausible video sequence, with the given source image serving as the first frame. While the source image implicitly guides the generation process, this constraint is not strictly enforced, so the generated first frame may slightly differ from the source image in some instances, as shown in Figure 7. Although this variation could indicate suboptimal generation quality, it is not considered a failure in the context of flow simulation. Instead, the generated first frame can still be paired with the source image for optical flow estimation, contributing to the diversity of the training data.

Limitation. The image-to-video generation process does not always fully replicate real-world video dynamics. For example, the generated video frames often lack continuous motion, resulting in unnatural motion dynamics. As shown in Figure 8, optical flow maps frequently exhibit checkerboard artifacts. This issue may stem from the patch-level copying of content between frames within the video generation model, possibly due to limitations in the video simulation process or the latent decoding mechanism.

Moreover, while multiple video frames are generated, they are used solely as target frames for optical flow generation, with the original image serving as the source frame. This limitation arises because only the transformed RGB images are available, preventing the newly generated frames

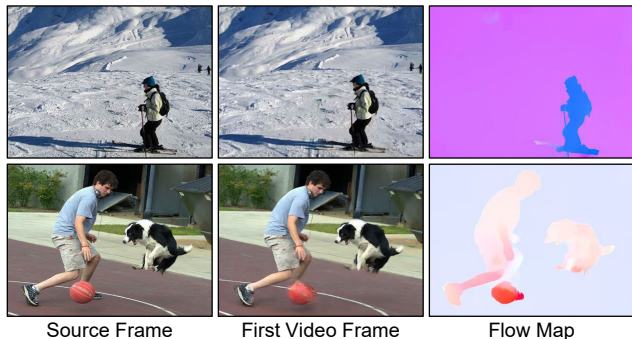


Figure 7. Visualization of the flow map generated between the source image and the first frame of the video.

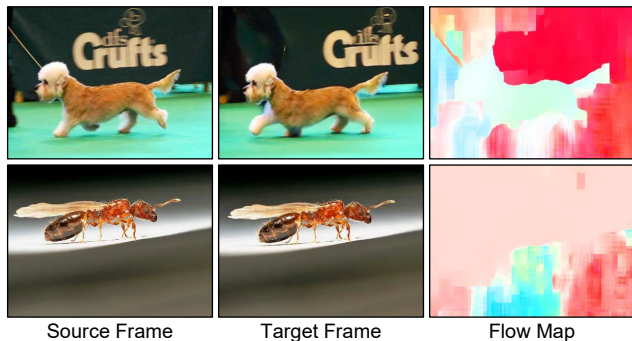


Figure 8. Visualization of the limitations of our simulated flows.

from being used as the source for optical flow calculation. If transformed segmentation masks could be generated concurrently with the RGB images during the image-to-video generation process, it would enable the creation of more diverse training data.

5. Conclusion

In this study, we investigate the use of large-scale image data to train flow-guided models. Rather than relying on source image distortion methods that fail to accurately mimic the optical flows of real video data, we demonstrate that novel image generation through image-to-video generation provides an effective solution. For the VSOD task, our approach sets a new state-of-the-art performance across all benchmark datasets, surpassing existing methods.

References

- [1] Radhakrishna Achanta, Sheila Hemami, Francisco Estrada, and Sabine Susstrunk. Frequency-tuned salient region detection. In *2009 IEEE conference on computer vision and pattern recognition*, pages 1597–1604. IEEE, 2009. **v**
- [2] Ali Athar, Sabarinath Mahadevan, Aljosa Osep, Laura Leal-Taixé, and Bastian Leibe. Stem-seg: Spatio-temporal embeddings for instance segmentation in videos. In *Computer Vision–ECCV 2020: 16th European Conference, Glasgow, UK, August 23–28, 2020, Proceedings, Part XI 16*, pages 158–177. Springer, 2020. **ii**
- [3] Andreas Blattmann, Tim Dockhorn, Sumith Kulal, Daniel Mendelevitch, Maciej Kilian, Dominik Lorenz, Yam Levi, Zion English, Vikram Voleti, Adam Letts, et al. Stable video diffusion: Scaling latent video diffusion models to large datasets. *arXiv preprint arXiv:2311.15127*, 2023. **iii**
- [4] Fred L Bookstein and WDK Green. A thin-plate spline and the decomposition of deformations. *Mathematical Methods in Medical Imaging*, 2(14-28):3, 1993. **ii**
- [5] Tim Brooks, Bill Peebles, Connor Holmes, Will DePue, Yufei Guo, Li Jing, David Schnurr, Joe Taylor, Troy Luhman, Eric Luhman, et al. Video generation models as world simulators. 2024. URL <https://openai.com/research/video-generation-models-as-world-simulators>, 3, 2024. **iii**
- [6] Yi-Wen Chen, Xiaojie Jin, Xiaohui Shen, and Ming-Hsuan Yang. Video salient object detection via contrastive features and attention modules. In *Proceedings of the IEEE/CVF winter conference on applications of computer vision*, pages 1320–1329, 2022. **v**
- [7] Ho Kei Cheng and Alexander G Schwing. Xmem: Long-term video object segmentation with an atkinson-shiffrin memory model. In *European Conference on Computer Vision*, pages 640–658. Springer, 2022. **ii**
- [8] Ho Kei Cheng, Yu-Wing Tai, and Chi-Keung Tang. Rethinking space-time networks with improved memory coverage for efficient video object segmentation. *Advances in Neural Information Processing Systems*, 34:11781–11794, 2021. **ii**
- [9] Ming-Ming Cheng, Niloy J Mitra, Xiaolei Huang, Philip HS Torr, and Shi-Min Hu. Global contrast based salient region detection. *IEEE transactions on pattern analysis and machine intelligence*, 37(3):569–582, 2014. **ii**
- [10] Suhwan Cho, Heansung Lee, Minhyeok Lee, Chaewon Park, Sungjun Jang, Minjung Kim, and Sangyoun Lee. Tackling background distraction in video object segmentation. In *European Conference on Computer Vision*, pages 446–462. Springer, 2022. **ii**
- [11] Suhwan Cho, Minhyeok Lee, Seunghoon Lee, Chaewon Park, Donghyeong Kim, and Sangyoun Lee. Treating motion as option to reduce motion dependency in unsupervised video object segmentation. In *Proceedings of the IEEE/CVF winter conference on applications of computer vision*, pages 5140–5149, 2023. **v, vi**
- [12] Suhwan Cho, Minhyeok Lee, Seunghoon Lee, Dogyoon Lee, Heeseung Choi, Ig-Jae Kim, and Sangyoun Lee. Dual prototype attention for unsupervised video object segmentation. In *Proceedings of the IEEE/CVF Conference on Computer Vision and Pattern Recognition*, pages 19238–19247, 2024. **iii**
- [13] Özgün Çiçek, Ahmed Abdulkadir, Soeren S Lienkamp, Thomas Brox, and Olaf Ronneberger. 3d u-net: learning dense volumetric segmentation from sparse annotation. In *Medical Image Computing and Computer-Assisted Intervention–MICCAI 2016: 19th International Conference, Athens, Greece, October 17–21, 2016, Proceedings, Part II 19*, pages 424–432. Springer, 2016. **iii**
- [14] Mark Everingham, Luc Van Gool, Christopher KI Williams, John Winn, and Andrew Zisserman. The pascal visual object classes (voc) challenge. *International journal of computer vision*, 88:303–338, 2010. **ii**
- [15] Deng-Ping Fan, Ming-Ming Cheng, Yun Liu, Tao Li, and Ali Borji. Structure-measure: A new way to evaluate foreground maps. In *Proceedings of the IEEE international conference on computer vision*, pages 4548–4557, 2017. **ii, v, vi**
- [16] Deng-Ping Fan, Wenguan Wang, Ming-Ming Cheng, and Jianbing Shen. Shifting more attention to video salient object detection. In *Proceedings of the IEEE/CVF conference on computer vision and pattern recognition*, pages 8554–8564, 2019. **ii, iv, v, vi, vii**
- [17] Jiaqing Fan, Tiankang Su, Kaihua Zhang, and Qingshan Liu. Bidirectionally learning dense spatio-temporal feature propagation network for unsupervised video object segmentation. In *Proceedings of the 30th ACM International Conference on Multimedia*, pages 3646–3655, 2022. **v**
- [18] Jiaqing Fan, Tiankang Su, Kaihua Zhang, Bo Liu, and Qingshan Liu. Temporally efficient gabor transformer for unsupervised video object segmentation. In *Proceedings of the 31st ACM International Conference on Multimedia*, pages 3394–3402, 2023. **v**
- [19] Yuchao Gu, Lijuan Wang, Ziqin Wang, Yun Liu, Ming-Ming Cheng, and Shao-Ping Lu. Pyramid constrained self-attention network for fast video salient object detection. In *Proceedings of the AAAI conference on artificial intelligence*, pages 10869–10876, 2020. **v**
- [20] Yuwei Guo, Ceyuan Yang, Anyi Rao, Maneesh Agrawala, Dahua Lin, and Bo Dai. Sparsectrl: Adding sparse controls to text-to-video diffusion models. In *European Conference on Computer Vision*, pages 330–348. Springer, 2025. **iii**
- [21] Bharath Hariharan, Pablo Arbeláez, Lubomir Bourdev, Subhransu Maji, and Jitendra Malik. Semantic contours from inverse detectors. In *2011 international conference on computer vision*, pages 991–998. IEEE, 2011. **ii**
- [22] Jonathan Ho and Tim Salimans. Classifier-free diffusion guidance. *arXiv preprint arXiv:2207.12598*, 2022. **iv**
- [23] Jonathan Ho, Ajay Jain, and Pieter Abbeel. Denoising diffusion probabilistic models. *Advances in neural information processing systems*, 33:6840–6851, 2020. **iii**
- [24] Ge-Peng Ji, Keren Fu, Zhe Wu, Deng-Ping Fan, Jianbing Shen, and Ling Shao. Full-duplex strategy for video object segmentation. In *Proceedings of the IEEE/CVF international conference on computer vision*, pages 4922–4933, 2021. **iii, v, vi**
- [25] Yuzhu Ji, Haijun Zhang, Zequn Jie, Lin Ma, and QM Jonathan Wu. Casnet: A cross-attention siamese network for video salient object detection. *IEEE transactions*

- on neural networks and learning systems, 32(6):2676–2690, 2020. **v**
- [26] Diederik P Kingma. Auto-encoding variational bayes. *arXiv preprint arXiv:1312.6114*, 2013. **iii**
- [27] Diederik P Kingma and Jimmy Ba. Adam: A method for stochastic optimization. *arXiv preprint arXiv:1412.6980*, 2014. **iv**
- [28] Pika Labs. Pika 1.0, 2023. <https://pika.art/>. **iii**
- [29] Minhyeok Lee, Suhwan Cho, Seunghoon Lee, Chaewon Park, and Sangyoun Lee. Unsupervised video object segmentation via prototype memory network. In *Proceedings of the IEEE/CVF winter conference on applications of computer vision*, pages 5924–5934, 2023. **iii**
- [30] Minhyeok Lee, Suhwan Cho, Dogyoon Lee, Chaewon Park, Jungho Lee, and Sangyoun Lee. Guided slot attention for unsupervised video object segmentation. In *Proceedings of the IEEE/CVF Conference on Computer Vision and Pattern Recognition*, pages 3807–3816, 2024. **iii**
- [31] Haofeng Li, Guanqi Chen, Guanbin Li, and Yizhou Yu. Motion guided attention for video salient object detection. In *Proceedings of the IEEE/CVF international conference on computer vision*, pages 7274–7283, 2019. **iii**
- [32] Jingyun Liang, Yuchen Fan, Kai Zhang, Radu Timofte, Luc Van Gool, and Rakesh Ranjan. Movidio: Motion-aware video generation with diffusion model. In *European Conference on Computer Vision*, pages 56–74. Springer, 2025. **iii**
- [33] Sabarinath Mahadevan, Ali Athar, Aljoša Ošep, Sebastian Hennen, Laura Leal-Taixé, and Bastian Leibe. Making a case for 3d convolutions for object segmentation in videos. *arXiv preprint arXiv:2008.11516*, 2020. **ii, v**
- [34] Peter Ochs, Jitendra Malik, and Thomas Brox. Segmentation of moving objects by long term video analysis. *IEEE transactions on pattern analysis and machine intelligence*, 36(6): 1187–1200, 2013. **ii, v, vi, vii**
- [35] Seoung Wug Oh, Joon-Young Lee, Kalyan Sunkavalli, and Seon Joo Kim. Fast video object segmentation by reference-guided mask propagation. In *Proceedings of the IEEE conference on computer vision and pattern recognition*, pages 7376–7385, 2018. **ii**
- [36] Seoung Wug Oh, Joon-Young Lee, Ning Xu, and Seon Joo Kim. Video object segmentation using space-time memory networks. In *Proceedings of the IEEE/CVF international conference on computer vision*, pages 9226–9235, 2019. **ii**
- [37] Youwei Pang, Xiaoqi Zhao, Lihe Zhang, and Huchuan Lu. Multi-scale interactive network for salient object detection. In *Proceedings of the IEEE/CVF conference on computer vision and pattern recognition*, pages 9413–9422, 2020. **v**
- [38] Gensheng Pei, Fumin Shen, Yazhou Yao, Guo-Sen Xie, Zhenmin Tang, and Jinhui Tang. Hierarchical feature alignment network for unsupervised video object segmentation. In *European Conference on Computer Vision*, pages 596–613. Springer, 2022. **v**
- [39] Federico Perazzi, Jordi Pont-Tuset, Brian McWilliams, Luc Van Gool, Markus Gross, and Alexander Sorkine-Hornung. A benchmark dataset and evaluation methodology for video object segmentation. In *Proceedings of the IEEE conference on computer vision and pattern recognition*, pages 724–732, 2016. **ii, iv, v, vi, vii**
- [40] Federico Perazzi, Anna Khoreva, Rodrigo Benenson, Bernt Schiele, and Alexander Sorkine-Hornung. Learning video object segmentation from static images. In *Proceedings of the IEEE conference on computer vision and pattern recognition*, pages 2663–2672, 2017. **ii**
- [41] Robin Rombach, Andreas Blattmann, Dominik Lorenz, Patrick Esser, and Björn Ommer. High-resolution image synthesis with latent diffusion models. In *Proceedings of the IEEE/CVF conference on computer vision and pattern recognition*, pages 10684–10695, 2022. **iii**
- [42] runway. Gen-2, 2023. <https://runwayml.com/research/gen-2>. **iii**
- [43] Hongje Seong, Junhyuk Hyun, and Euntai Kim. Kernelized memory network for video object segmentation. In *Computer Vision—ECCV 2020: 16th European Conference, Glasgow, UK, August 23–28, 2020, Proceedings, Part XXII 16*, pages 629–645. Springer, 2020. **ii**
- [44] Hongje Seong, Seoung Wug Oh, Joon-Young Lee, Seongwon Lee, Suhyeon Lee, and Euntai Kim. Hierarchical memory matching network for video object segmentation. In *Proceedings of the IEEE/CVF International Conference on Computer Vision*, pages 12889–12898, 2021. **ii**
- [45] Jianping Shi, Qiong Yan, Li Xu, and Jiaya Jia. Hierarchical image saliency detection on extended cssd. *IEEE transactions on pattern analysis and machine intelligence*, 38(4): 717–729, 2015. **ii**
- [46] Jiaming Song, Chenlin Meng, and Stefano Ermon. Denoising diffusion implicit models. *arXiv preprint arXiv:2010.02502*, 2020. **iii**
- [47] Yang Song and Stefano Ermon. Improved techniques for training score-based generative models. *Advances in neural information processing systems*, 33:12438–12448, 2020. **iv**
- [48] Tiankang Su, Huihui Song, Dong Liu, Bo Liu, and Qingshan Liu. Unsupervised video object segmentation with online adversarial self-tuning. In *Proceedings of the IEEE/CVF International Conference on Computer Vision*, pages 688–698, 2023. **v**
- [49] Yukun Su, Jingliang Deng, Ruizhou Sun, Guosheng Lin, Hanjing Su, and Qingyao Wu. A unified transformer framework for group-based segmentation: Co-segmentation, co-saliency detection and video salient object detection. *IEEE Transactions on Multimedia*, 26:313–325, 2023. **v**
- [50] Zachary Teed and Jia Deng. Raft: Recurrent all-pairs field transforms for optical flow. In *Computer Vision—ECCV 2020: 16th European Conference, Glasgow, UK, August 23–28, 2020, Proceedings, Part II 16*, pages 402–419. Springer, 2020. **iv, v**
- [51] Lijun Wang, Huchuan Lu, Yifan Wang, Mengyang Feng, Dong Wang, Baocai Yin, and Xiang Ruan. Learning to detect salient objects with image-level supervision. In *Proceedings of the IEEE conference on computer vision and pattern recognition*, pages 136–145, 2017. **iv**
- [52] Wenguan Wang, Jianbing Shen, and Ling Shao. Consistent video saliency using local gradient flow optimization and global refinement. *IEEE Transactions on Image Processing*, 24(11):4185–4196, 2015. **ii, v, vi, vii**

- [53] Wenguan Wang, Jianbing Shen, and Ling Shao. Video salient object detection via fully convolutional networks. *IEEE Transactions on Image Processing*, 27(1):38–49, 2017. [ii](#)
- [54] Jun Wei, Shuhui Wang, and Qingming Huang. F³net: fusion, feedback and focus for salient object detection. In *Proceedings of the AAAI conference on artificial intelligence*, pages 12321–12328, 2020. [v](#)
- [55] Sanghyun Woo, Jongchan Park, Joon-Young Lee, and In So Kweon. Cbam: Convolutional block attention module. In *Proceedings of the European conference on computer vision (ECCV)*, pages 3–19, 2018. [iv](#)
- [56] Enze Xie, Wenhai Wang, Zhiding Yu, Anima Anandkumar, Jose M Alvarez, and Ping Luo. Segformer: Simple and efficient design for semantic segmentation with transformers. *Advances in neural information processing systems*, 34: 12077–12090, 2021. [iv](#), [vii](#)
- [57] Shu Yang, Lu Zhang, Jinqing Qi, Huchuan Lu, Shuo Wang, and Xiaoxing Zhang. Learning motion-appearance co-attention for zero-shot video object segmentation. In *Proceedings of the IEEE/CVF international conference on computer vision*, pages 1564–1573, 2021. [iii](#)
- [58] Zhao Yang, Qiang Wang, Luca Bertinetto, Weiming Hu, Song Bai, and Philip HS Torr. Anchor diffusion for unsupervised video object segmentation. In *Proceedings of the IEEE/CVF international conference on computer vision*, pages 931–940, 2019. [v](#)
- [59] Shengming Yin, Chenfei Wu, Jian Liang, Jie Shi, Houqiang Li, Gong Ming, and Nan Duan. Dragnuwa: Fine-grained control in video generation by integrating text, image, and trajectory. *arXiv preprint arXiv:2308.08089*, 2023. [iii](#)
- [60] Shiwei Zhang, Jiayu Wang, Yingya Zhang, Kang Zhao, Hangjie Yuan, Zhiwu Qin, Xiang Wang, Deli Zhao, and Jingren Zhou. I2vgen-xl: High-quality image-to-video synthesis via cascaded diffusion models. *arXiv preprint arXiv:2311.04145*, 2023. [iii](#)
- [61] Xiaoqi Zhao, Youwei Pang, Lihe Zhang, Huchuan Lu, and Lei Zhang. Suppress and balance: A simple gated network for salient object detection. In *Computer Vision—ECCV 2020: 16th European Conference, Glasgow, UK, August 23–28, 2020, Proceedings, Part II 16*, pages 35–51. Springer, 2020. [v](#)
- [62] Mingmin Zhen, Shiwei Li, Lei Zhou, Jiaxiang Shang, Haoan Feng, Tian Fang, and Long Quan. Learning discriminative feature with crf for unsupervised video object segmentation. In *Computer Vision—ECCV 2020: 16th European Conference, Glasgow, UK, August 23–28, 2020, Proceedings, Part XXVII 16*, pages 445–462. Springer, 2020. [v](#)
- [63] Tianfei Zhou, Shunzhou Wang, Yi Zhou, Yazhou Yao, Jianwu Li, and Ling Shao. Motion-attentive transition for zero-shot video object segmentation. In *Proceedings of the AAAI conference on artificial intelligence*, pages 13066–13073, 2020. [iii](#)